Bragg coherent diffraction imaging by simultaneous reconstruction of multiple diffraction peaks

Yuan Gao, Xiaojing Huang, Hanfei Yan, and Garth J. Williams

Title:

Bragg coherent diffraction imaging by simultaneous reconstruction of multiple diffraction peaks

Authors:

Yuan Gao[*], Xiaojing Huang, Hanfei Yan, and Garth J. Williams[*]

National Synchrotron Light Source II, Brookhaven National Laboratory, Upton, NY 11973, USA

[*]*Email: yuangao@bnl.gov; gwilliams@bnl.gov*

Corresponding author:

Yuan Gao,
Brookhaven National Laboratory, Building 743, Upton, NY 11973-5000.
Phone 631 344-3781, Email: yuangao@bnl.gov

Abstract:

Bragg coherent diffractive imaging (BCDI) is a non-invasive microscopy technique that can visualize the morphology and internal lattice deviations of crystals with nanoscale spatial resolution and picometer deformation sensitivity. While BCDI has been successfully applied in various studies of materials, it is less successful for highly-strained crystals. Specifically, it is difficult to correctly reconstruct the electron density of a highly-strained object using conventional phase retrieval algorithms. Although various algorithms have been developed to overcome this challenge, most of them require *a priori* knowledge that is not always available in practice. Here we report on a new phase retrieval workflow that can invert diffraction patterns from multiple Bragg peaks simultaneously. The new workflow is explored via simulated diffraction from crystals with various strain conditions. Reconstructions from the new workflow consistently demonstrate more accurate electron density maps, in comparison with the conventional method. For highly-strained crystals, the new workflow improves the reliability and consistency of BCDI phase retrieval significantly.

I. Introduction

Strain describes the spatial deformations of a crystal structure from its ground state. It is connected to the internal stress of the crystal through elasticity theory and has a tensorial nature. For decades, strain has been known as an effective mechanism for manipulating the physical and chemical properties of materials [1–3]. Specifically, nanostructured materials can withstand much larger strain in comparison with bulk materials, leading to new possibilities for tuning the functional properties. Developing the imaging capability that can quantitatively monitor the strain field in nanomaterials is essential for modern materials science.

Bragg coherent diffractive imaging (BCDI) [4–7] is a non-invasive strain probing technique that can measure the 3D strain fields of finite crystals with nanometer spatial resolution and picometer-scale deformation sensitivity. Utilizing iterative phase retrieval algorithms, diffraction from a strained crystal can be inverted to a complex object function, where the magnitude represents the effective electron density distribution of the crystal, and the phase represents a projection of the lattice deviations to the momentum transfer vector of the measured Bragg peak. Similar to the other coherent diffractive imaging (CDI) techniques [8–12], the resolution of BCDI is based on the wavelength of the illumination and the largest scattering angle recorded, rather than the image-forming lens [13–15].

Various iterative algorithms have been developed to invert the diffraction patterns [16–18]. However, since phase retrieval is a nonlinear and nonconvex optimization problem, error minimization strategies are prone to stagnation due to the presence of local minima. Specifically, BCDI is less successful for highly strained crystals, which are defined in the continuum limit as the real-space phase exceeds the range of $\pm\pi/2$ [19,20]. The retrieved object usually shows an unphysical electron density map with a "gap" in the region of strong phases. Special algorithms have been developed to better reconstruct highly-strained crystals. For example, Newton et al. [19] applied an additional density normalizing algorithm to the regular hybrid input-output (HIO) algorithm [16], in order to acquire a uniform electron density in the reconstruction. In another work, Huang et al. [20] performed phase-constrained HIO several times to obtain a reasonable support, then ran regular HIO using this refined support to correctly reconstruct the object. However, both methods require *a priori* knowledge – knowing that the crystals should not have discontinuity in electron density – that is not always available.

In practice, one could improve the reliability and consistency of the convergence of iterative phase retrieval by increasing data redundancy, such as the overlap constraint in ptychography [11,12]. Conventional BCDI is based on a single Bragg peak, resulting in limited data redundancy. Although it

has been shown that reconstructions from multiple diffraction peaks can be combined together to retrieve the strain tensor [21], the multiple peaks were inverted separately rather than treated as one dataset. While the independently reconstructed objects can be considered as a consistency validation, it may introduce extra errors associated with alignment, as the projection from Fourier-space to real-space is insensitive to translation. Recently, Newton [22] proposed a concurrent approach to eliminate such alignment-induced artifacts by reconstructing the strain field concurrently with the iterative phase retrieval. Meanwhile, Wang et al. [23] proposed a new algorithm to reconstruct highly-strained crystals that are undergoing phase transformations. The new approach simultaneously inverts multiple scans of the same Bragg peak from a particle at different states, assuming that the shape of the particle does not change while the structure phases are evolving. Although this method fits well with some *in situ* and operando studies, it may not be implemented in more general cases.

In this paper, we use simulated Bragg diffraction from strained crystals to demonstrate that multiple Bragg peaks can be treated as one dataset and simultaneously inverted using a modified workflow based on the established error reduction (ER) and HIO algorithms [16]. In the obtained object, the deformation can be completely determined if proper Bragg peaks were selected. In the case of a highly-strained crystal, the object can be correctly reconstructed in a single run without *a priori* knowledge.

II.   Forward modeling and phase retrieval method

A.   Bragg diffraction simulation

All diffraction simulations presented in this paper were performed in the kinematic diffraction regime [24]. We considered only the elastic scattering of X-rays, while the other effects – such as absorption, inelastic scattering, refraction, and partial coherence effect – were excluded. We also ignored instrument effects, such as the detector counting statistics or background scattering.

The diffraction intensity of a crystal is determined by the square of the crystal form factor, which is a function of the momentum transfer vector $\boldsymbol{q} = \boldsymbol{k}_f - \boldsymbol{k}_i$ [25]:

$$A(\boldsymbol{q}) = \sum_{n=1}^{N} f_n(\boldsymbol{q}) \exp[-\mathrm{i}(\boldsymbol{q} \cdot \boldsymbol{r}_n)] \ \#(1)$$

where $\boldsymbol{k}_i$ and $\boldsymbol{k}_f$ are the wavevectors of incident and diffracted photons, respectively. The vector $\boldsymbol{r}_n$ defines the coordinate of atom n with respect to an arbitrary origin. The summation is performed over all atoms N in the crystal. $f_n(\boldsymbol{q})$ is the atomic form factor of atom n, which depends on the type of the atom and the scattering angle defined by $\boldsymbol{q}$.

In this study, we chose Ag crystals with a face-centered cubic lattice as the object. The atomic form factor was taken from the Xraylib library [26]. For a crystal with a specific shape, the coordinates of all atoms in a perfect lattice were first calculated with respect to the geometric center of the crystal. A deformation vector was then added to $\boldsymbol{r}_n$, if the nth atom was displaced from its ideal lattice position. Finally, the crystal was rotated to satisfy the Bragg condition by applying a rotation matrix to each member of the set $\{\boldsymbol{r}_n\}$. Since Eq. 1 is computationally expensive, the maximum number of unit cells in the Ag crystal is 60 × 60 × 60, which is approximately 25 × 25 × 25 nm³ in size.

The diffraction intensity was calculated in a volume of reciprocal space surrounding a Bragg peak, mimicking a rocking curve scan with an illumination wavelength of 1 Å, a sample-detector distance of 0.25 m, and a pixel size of 220 µm. These parameters are dictated by several factors, including the spatial sampling rate, the detection dynamic range, and the largest scattering angle. A detailed discussion is given in Appendix A.

The schematic diagram of a typical rocking curve scan is presented in Fig. 1(a). To evaluate the performance of the new workflow, we simulated the diffraction from Ag crystals under two

conditions: a "low-strain" case and a "high-strain" case. In the former case, we generated a cubic crystal with Lorentzian-shaped defects. As shown in Fig. 1(b), all the six defects are centered on a y'-z' plane passing through the center of the crystal, while the displacements are along different axes with a maximum magnitude of 10% of the lattice constant. As for the "high-strain" case shown in Fig. 1(c), a square-frustum-shaped crystal was generated, with only one screw dislocation along the x' direction. In both cases, the following diffraction patterns were simulated: [111], [$\overline{1}11$], [200], [020], [002], [220], [202], [022], [311], [131], and [113].

B.   Simultaneous phase retrieval of multiple diffraction peaks

Iterative algorithm in CDI can be expressed in a projector notation [17,18], including the modulus constraint π_m, the support constraint π_s, and the complex object function $o^{(k)}$. Using this notation, ER can be expressed as

$$o^{(k+1)} = (\pi_s\pi_m)o^{(k)} \quad \#(2)$$

while HIO is

$$o^{(k+1)} = [(1 - \pi_s)(1 - \beta\pi_m) + \pi_s\pi_m]o^{(k)} \quad \#(3)$$

where β is the HIO parameter. $\pi_m o^{(k)}$ is the best estimate of the object on the kth iteration.

For Bragg scattering, the 3D diffraction pattern is sampled by the Ewald sphere in a skewed coordinate system [27]. In conventional BCDI, the iterative reconstruction is performed in the detector frame, followed by one coordinate transformation at the end to acquire the object in the crystal frame. For the new workflow, however, we need to transform the object between the crystal frame and multiple detector frames in each iteration. We introduce a coordinate transformation projector, T, where $T^{d\to c}$ is the transformation from a detector frame to the crystal frame and $T^{c\to d}$ is its inverse. Details of this projector are discussed in Appendix B. We can write ER and HIO to explicitly apply the support constraint in the crystal frame:

$$o'^{(k)}_j = \left(\pi_s T_j^{d\to c}\pi_m T_j^{c\to d}\right)o_j^{(k)} \quad \#(4)$$
$$o'^{(k)}_j = [(1 - \pi_s)T_j^{d\to c}(1 - \beta\pi_m)T_j^{c\to d} + \pi_s T_j^{d\to c}\pi_m T_j^{c\to d}]o_j^{(k)} \quad \#(5)$$

where $j = 1,2,\dots M$ are different Bragg peaks.

The magnitude of $o^{(k)}$, i.e., electron density of the crystal, should be identical for all Bragg peaks. The phase, however, represents different projections of the deformation, $\boldsymbol{U}$. The phase of voxel i of $o^{(k)}$ from Bragg peak j, ψ_{ij}, is linked to the crystal deformation by $\psi_{ij} = \widehat{\boldsymbol{Q}}_j\widehat{\boldsymbol{U}}_i$, where $\widehat{\boldsymbol{Q}}_j$ is the matrix representation of the momentum transfer vector of Bragg peak j, and $\widehat{\boldsymbol{U}}_i$ is the matrix representation of the displacement vector of voxel i.

The magnitude and phase of $o^{(k)}$ need to be treated separately when combining different peaks together. We define the transformation from one peak to another as

$$o_{i,j+1}^{(k)} = \left|o'^{(k)}_{i,j}\right|\exp[\mathrm{i}(\widehat{\boldsymbol{Q}}_{j+1}\widehat{\boldsymbol{U}}_i)] \quad \text{for } j = 1,2,\dots,\mathrm{M} - 1$$
$$o_{i,1}^{(k+1)} = \left|o'^{(k)}_{i,j}\right|\exp[\mathrm{i}(\widehat{\boldsymbol{Q}}_1\widehat{\boldsymbol{U}}_i)] \qquad \text{for } j = \mathrm{M} \quad \#(6)$$

It is necessary to simultaneously solve $\boldsymbol{U}$ during the iterative phase retrieval. Inspired by the bisection method [28], we define an iterative procedure

$$\widehat{\boldsymbol{U}}_i^{(k,j+1)} = \widehat{\boldsymbol{U}}_i^{(k,j)} + \widehat{\boldsymbol{Q}}_j^+\left\{\arg\left[o'^{(k)}_{i,j}\right] - \widehat{\boldsymbol{Q}}_j\widehat{\boldsymbol{U}}_i^{(k,j)}\right\} \quad \#(7)$$

where $\widehat{\boldsymbol{Q}}_j^+$ is the Moore-Penrose pseudoinverse [29] of $\widehat{\boldsymbol{Q}}_j$, satisfying $\widehat{\boldsymbol{Q}}_j^+\widehat{\boldsymbol{Q}}_j = \boldsymbol{I}$. The initial $\boldsymbol{U}$ is zero-valued. For peak j on the kth iteration, Eq. 7 finds the difference between the phase of the object after modulus and support constraints, $o'^{(k)}_j$, and the phase derived from the current estimate of the deformation, $\widehat{\boldsymbol{Q}}_j\widehat{\boldsymbol{U}}^{(k,j)}$. Then, $\boldsymbol{U}$ is updated, assuming the lattice displacements along three different axes equally contribute to such difference in phase. As discussed in a previous study [30], $\boldsymbol{U}$ can be fully retrieved if 3 reflections with linearly independent $\boldsymbol{Q}$ vectors are measured, while collecting more reflections results in a higher over-determination ratio and decreases the uncertainty of the measurements.

In this study, various combinations of 4 diffraction peaks with non-planar $\boldsymbol{Q}$ vectors were inverted. The simulated diffraction intensity with a random phase was used as the starting point of the phase retrieval. The initial support box was 50% of the input array and filled with a constant real density. Shrinkwrap [31] was implemented to refine the support using a Gaussian blurring function with a sigma of 1 voxel and 20% cutoff threshold. For all reconstructions, 250 iterations were carried out with 200 iterations of simultaneous phase retrieval and 50 iterations of individual phase retrieval. The first 200 iterations were performed by alternating between ER and HIO. The remaining 50 iterations used ER with 10 iterations in the crystal frame followed by 40 iterations without coordinate transformation to eliminate the numerical error introduced by interpolations. $\boldsymbol{U}$ was updated every 5 iterations from 21st to 200th iteration. For iterations on which $\boldsymbol{U}$ was not updated, the phase terms in Eq. 6 were from corresponding peaks in the previous iteration. The final object of each peak was obtained from the last estimate, $\pi_m o_j^{(250)}$, without averaging.

III.   Analysis of the reconstructions

In this section, we evaluate the performance of the new workflow. We call the conventional workflow the "individual-peak approach" (IP) and the modified workflow the "multiple-peak approach" (MP). The parameters of ER and HIO in IP are identical to those in MP. Objects reconstructed from two approaches are compared to the ground truth by visual inspection and the reciprocal-space χ-squared error metric. For the high-strain cases, the success rates of reconstruction are also reported.

A.   Reconstructions of low-strain objects

The low-strain case is aimed to reveal potential numerical artifacts that the new workflow could induce. Since the crystal contains only minor deformation, MP of any 4 diffraction peaks with non-planar $\vec{q}$ vectors can reconstruct the object correctly. Alternating the sequence of peaks in MP does not show any significant change in the reconstruction quality (see Appendix C). Here, reconstructions from [311] are demonstrated as a representative example.

[311] was inverted with [002], [220], and [$\overline{1}1\overline{1}$] in MP. Fig. 2(a) and 2(b) show a typical reconstruction. Both the shape and size of the crystal are reconstructed accurately, and the magnitude inside the crystal is relatively uniform. Comparing Fig. 2(b) with Fig. 1(b), the crystal deformation is clearly revealed in the phase map. The phase changes induced by deformation along x' are approximately three times of those induced by deformation in y' and z', which is consistent with the magnitude of the components of the momentum associated with [311] peak. Using IP, the shape and size are also reconstructed correctly, but obvious errors in the magnitude of the reconstructed crystal are observed. As shown in Fig. 2(e)-(h), these magnitude errors are spatially correlated to the deformation along x', suggesting that they are induced by the strong phases.

Fig. 3(a) shows the behaviors of χ^2 during MP reconstruction. The χ^2 of all 4 peaks converge to a value below 0.01 after switching from HIO to ER for the first time. The following iterations do not show a significant change in χ^2 until the 200th iteration, except the second round of HIO. The first round of HIO and the update of $\boldsymbol{U}$ started from the 21st iteration, resulting in a fast converging of χ^2 in a few iterations. In the following iterations, the converged $\boldsymbol{U}$ only causes minor increases in χ^2. Two notable decreases in χ^2 are seen at the 201st and 211th iterations, respectively. The former corresponds to the switch from simultaneous phase retrieval to individual phase retrieval in the crystal frame, indicating that transformations from one peak to another introduce extra errors. These transformation-induced errors, as well as the $\boldsymbol{U}$-induced errors mentioned above, are linked to the numerical error caused by interpolating the object from one peak to another, namely a "mismatch" between any two Bragg peaks (see Appendix C). The latter decrease at the 211th iteration is because of ceasing the coordinate transformation in the individual phase retrieval, indicating the numerical

error induced by interpolation itself. The final χ^2 values of MP are very close to the ones of IP, although the reconstructions from MP do not exhibit the magnitude errors seen in IP.

B. Reconstructions of high-strain objects

For the high-strain case, we present the reconstructions of [022], [$\overline{1}\overline{1}\overline{1}$], [002], and [200]. While most algorithm settings are identical to the ones in the low-strain case, U updating starts from the 61st iteration instead of the 21st. Since [022] and [002] are insensitive to the screw dislocation along x' direction, the objects retrieved from these two peaks should be deformation free. The reconstructions of dislocation-sensitive peaks – [$\overline{1}\overline{1}\overline{1}$] and [200] in this case – should show a circular phase wrap around the axis of the screw dislocation. As shown in Fig. 4, both IP and MP can invert [022], [$\overline{1}\overline{1}\overline{1}$], and [002] accurately. As for [200], while the reconstruction from MP is still accurate, IP cannot obtain the correct magnitude or phase of the truth object.

In Fig. 4(b), reconstructions of [$\overline{1}\overline{1}\overline{1}$] and [200] show a cylindrical volume of low electron density, which spatially overlaps with the axis of the screw dislocation. This is commonly seen in crystals containing screw dislocations [32]. Their phases are circularly wrapped in opposite directions, consistent with their momentum transfer vectors. Comparing the phase maps of [200] and [$\overline{1}\overline{1}\overline{1}$] with the displacement map shown in Fig. 1(c), the locations of sharp discontinuities are different from those in the truth object. This is not surprising since this location can be rotated around the dislocation axis by adding a global phase offset [33]. The simultaneous phase retrieval is able to lock the dislocation at the same spatial position in different reflections. However, the individual phase retrieval in the end of the iterative process eliminates the constraint, allowing different reflections to have arbitrary global phase offsets. It is also worth mentioning that the discontinuities shown in the phase of [200] are slightly curved, suggesting the presence of a phase ramp. This can be eliminated by centering the object's Fourier transform in the Fourier-space volume.

The behaviors of χ^2 of the high-strain case are shown in Fig. 3(b). Similar to the low-strain case, χ^2 converges in less than 70 iterations. However, unlike the low-strain case, χ^2 of all 4 peaks stagnate at relatively high levels, while [200] has the highest value. After switching from simultaneous phase retrieval to individual phase retrieval at the 201st iteration, χ^2 decreases from 0.05 - 0.2 to around 0.005. Both the stagnations and the dramatic decreases, as well as the larger U-induced errors, indicate that the "mismatch" mentioned earlier plays a significant role in the numerical error (see Appendix C). At the 211th iteration, ceasing the coordinate transformation results in a further decrease from 0.005 to 0.002.

We also monitored the success rates of IP and MP in the high-strain case. As shown in Table I, three dislocation-sensitive peaks, [$\overline{1}\overline{1}\overline{1}$], [200], and [311], were inverted respectively with random seeds for 20 trials using IP. Surprisingly, reconstructions of [$\overline{1}\overline{1}\overline{1}$] show a success rate as high as 90%. The success rates drop to 0% for both [200] and [311], because of the strong phase present in the truth objects corresponding to those peaks. Employing MP, various combinations of 4 peaks were inverted with random seeds for 10 trials. Two types of combinations were tested. In one type, only one dislocation-sensitive peak was combined with three dislocation-insensitive peaks. A success rate of 100% is achieved for a combination containing [$\overline{1}\overline{1}\overline{1}$], while the success rate of a combination containing [200] is 50%. In the other type, two dislocation-sensitive peaks were mixed with two dislocation-insensitive peaks. The combination of [$\overline{1}\overline{1}\overline{1}$] and [200] gives a 70% success rate, while the one of [$\overline{1}\overline{1}\overline{1}$] and [311] has a 60% success rate. The lowest success rate, 30%, is from the combination of [200] and [311]. We notice that alternating the sequence of the 4 peaks used as a particular dataset does not affect the success rate significantly.

IV. Discussion

Table I clearly demonstrates that the new workflow has better performance in the case of highly-

strained objects. While [$\overline{111}$] can be inverted by IP with a reasonable success rate, the reconstruction using [200] or [311] is unreliable. As a comparison, combining [200] with dislocation-insensitive peaks dramatically improves the success rate, as the electron density is forced to converge to the truth object. Adding [$\overline{111}$] to the combination can further increase the success rate due to the use of an iteratively updated $\widehat{U}$: since the truth object corresponding to [$\overline{111}$] is reliably recovered, the phases retrieved from [$\overline{111}$] and the other two dislocation-insensitive peaks are enough to reconstruct U. With the assistance of U, it is much easier to solve the phase ambiguities in [200] and [311].

The new workflow has another advantage that the dislocation-sensitive peaks can be identified by monitoring χ^2. As shown in Fig. 3(b), [200] peak, which has the strongest phase among the four peaks, shows the highest χ^2 value in all MP iterations. Higher χ^2 values are observed when inverting peaks including [311], as shown in Fig. A3 and A4. Utilizing this feature, we can define a weighted multiple-peak approach, in which the dislocation-insensitive peaks dominate the reconstruction of the electron density. Assigning non-uniform weighting factors in the estimation of U is more likely to result in the correct shape of the crystal and facilitate the resolution of any phase ambiguities in the dislocation-sensitive peaks.

The new workflow not only improves the reliability of phase retrieval but also enhance the effective sensitivity of crystal deformation. In BCDI, diffraction peaks with larger momentum transfer vectors are more sensitive to the deformation. However, when applying BCDI on highly-strained crystals, such peaks are usually not selected, since they exhibit strong phases and cannot be reliably inverted. In the new workflow, diffraction peaks with different levels of sensitivity can be inverted together. Therefore, one can measure large deformation with high sensitivity, which is challenging in conventional BCDI.

A practical challenge of the new workflow is the computation requirement. Due to the numerous interpolations, the new workflow is more time-consuming than the conventional method. A detailed discussion is given in Appendix D.

V. Conclusion

In summary, we propose a new BCDI phase retrieval workflow that can reliably reconstruct highly-strained crystals by inverting multiple diffraction peaks simultaneously. We have tested the workflow on simulated particles with different morphologies and strain levels. By combining peaks that have different levels of sensitivity of crystal deformation, the new workflow significantly increases the success rate of phase retrieval. The displacement field of the crystal can be fully resolved if proper Bragg peaks were selected, allowing complete determination of the strain tensor. Meanwhile, the reconstructions obtained from the new workflow show more accurate electron density maps, in comparison with those from conventional BCDI phase retrieval. Our workflow provides a reliable method to perform BCDI on nanomaterials exhibiting large strains and complicated phase structures. We expect that this method will find widespread applications to functional nanomaterials under working conditions or in extreme environments, such as energy storage and conversion materials [34], electronic or micromechanical devices [35,36], and engineered catalysts [2,37].

Acknowledgements

Appendix A: Experiment parameters of BCDI simulations

In this study, the diffraction data are simulated to mimic the realistic BCDI experimental conditions, while the inherent instrument errors are ignored. Limited by the computing resource, the simulated datasets are 64 × 64 × 64 matrices, corresponding to a 64-frame rocking-curve scan with 64 × 64 pixels on each frame.

For a BCDI measurement, several factors are critical, such as the spatial sampling rate, the data dynamic range, the largest scattering angle that needs to be recorded, and the aliasing effect. These factors determine the experiment parameters including illumination wavelength, detector pixel size, sample-detector distance, and the angular step of the rocking-curve scan. This section provides a detailed discussion of all these factors.

Spatial sampling rate. CDI requires that the diffraction intensity is sampled above the Nyquist frequency [38]. Although it has been shown that 3D objects can be successfully reconstructed using an oversampling ratio as low as 2.57 [39], recent work demonstrated that a higher oversampling ratio can improve the quality of reconstructions [40]. To eliminate the potential risk of deficient sampling, we set an oversampling ratio above 3 in each dimension, resulting in a 3D oversampling ratio of more than 40.

Data dynamic range. Due to the well-known Q^{-4} power-law decay of the diffraction signal [41], the dynamic range of the intensity data determines the quality of the accessible information in a diffraction experiment. In practical experiments, data dynamic range is commonly dictated by the radiation dose limits of samples, temporal constraints of data collection, and the photon dynamic ranges of detectors. However, in this simulation study, we only consider the effect of deficient data dynamic range on the quality of reconstructed objects. Öztürk et al. [40] have shown that an order of 6 in dynamic range is necessary for the intensity measurements to reach ultimate reconstruction performance. To be conservative, we set the dynamic range of simulated diffraction data to 10^7. The diffraction pattern from a perfect crystal was generated as a reference. The maximum pixel intensity was fixed to 10^7 photons, and the intensities of rest pixels were rounded to non-negative integer numbers. Then, diffraction patterns from strained crystals were normalized to the reference using integrated intensity.

Largest scattering angle. The largest scattering angle in the simulated diffraction data affects the spatial resolution of the reconstructed objects. The half-period resolution of a CDI measurement, Δx, is dictated by the illumination wavelength, λ, and the largest scattering angle of the collected diffraction signal, θ_{max}, by $\Delta x = \frac{\lambda}{2 \sin{(\theta_{max})}}$. In this study, since the simulated sample crystals are around 25 × 25 × 25 nm³, a spatial resolution of 2.5 nm or less is necessary to obtain reasonably good reconstructions. Meanwhile, the required oversampling ratio and the size of the data array set an upper limit on the scattering angle. In the third dimension, the spatial resolution is linked to the angular step of the rocking curve scan, as well as the momentum transfer vector of the Bragg peak.

Aliasing effect. This effect can occur when the continuous boundary conditions of the Fourier transform are violated as the diffraction intensity does not completely decay to zero within the detection range. Since the diffracted power decays with spatial frequency, this effect also affects

θ_{max} and the data dynamic range.

Taking account of all factors discussed above, we set θ_{max} to 1.5° in both directions of the detector plane. The corresponding real-space in-plane resolution is approximately 1.9 nm in both directions. The detector pixel size is 220 μm for a sample-detector distance of approximately 0.25 m and an illumination wavelength of 1 Å. For each Bragg peak, a proper angular step was selected so that the spatial resolution in the third dimension is the same as the in-plane resolution.

The aliasing effect in the reconstruction is evaluated by zero-padding the data [42]. Diffraction simulations of [002], [220], [311], and [$\overline{111}$] from the low-strain crystal are zero-padded from 64 × 64 × 64 matrices to 96 × 96 × 96 matrices. The padded arrays were reconstructed using the multiple-peak approach described in the main text. The obtained objects were compared with the ones reconstructed from the original arrays, using visual inspection and the χ-squared error metric. We did not observe any notable change in the quality of the reconstruction except a resolution effect, as the spatial resolution is artificially improved due to zero-padding.

Appendix B: Coordinate transformation in BCDI

In a typical rocking curve scan, the coherent diffraction pattern is measured by sweeping the Ewald sphere through the Bragg peak. The obtained 3D diffraction intensity, which is sampled uniformly on an orthogonal grid in the detector frame, is actually on a non-uniform oblique grid when transformed to the crystal frame. Thus, one obtains a skewed object by directly inverting the collected diffraction data. In conventional BCDI, the skewed object can be corrected via coordinate transformation. Such methods exist in literatures [27,43–45].

Our coordinate transformation method follows the same logic as those described above, with a slight alteration aimed at reducing computation time. The traditional method is computationally expensive due to the interpolation of 3D scattered data. This is prohibitively time-consuming in the proposed workflow, since the dataset from each Bragg peak must be interpolated twice in every iteration. To accelerate the process, we move the 3D interpolation to the detector frame by mapping the orthogonal grid in the crystal frame to a new oblique grid in the detector frame. As a result, the data that needs to be interpolated becomes a gridded array, reducing the computational complexity dramatically. For example, it typically takes 7-10 seconds to interpolate a scattered 64 × 64 × 64 complex array, while the interpolation of a gridded array in the same size takes only about 0.5 seconds.

The curvature of the Ewald sphere is also considered in our coordinate transformation method. A rocking curve scan can be imagined as slicing the 3D coherent diffraction pattern with the Ewald sphere. Traditionally, these slices are approximated to a set of sheared parallel planes in the reciprocal space, where the shearing effect is from the non-orthogonal nature of the rocking curve scan [6,45,46]. This approximation is valid when the length scale of the sampled reciprocal space is much smaller than the momentum transfer vector of the Bragg peak. With this approximation, the coordinate transformation is simply a linear transformation from non-orthogonal bases in the reciprocal space to orthogonal bases in the real space. However, this approximation is not necessarily valid for our simulations due to the large scattering angles.

To investigate whether the approximation is valid in this study, we tested the coordinate transformation and its inverse on an object reconstructed from the [111] diffraction of a rectangular-prism-shaped crystal. Fig. A1(a) shows the object obtained by directly inverting the [111] diffraction pattern. Since the object is in the detector frame, slices through the object reveal significant shearing

effects. Fig. A1(b) demonstrates the object after applying the linear coordinate transformation, i.e. the Ewald sphere is approximated to a flat plane when calculating the coordinates in reciprocal space. As a comparison, the object in Fig. A1(c) is obtained from a coordinate transformation that takes the curvature of the Ewald sphere into account. Obviously, the object in Fig. A1(b) is still skewed, while the object in Fig. A1(c) is transformed correctly. Fig. A1(d) and A1(e) show the objects after applying the inverse transformation with and without the approximation, respectively. Both look almost identical to the original object shown in Fig. A1(a).

Appendix C: Numerical errors introduced by 3D interpolation

To evaluate the numerical error introduced by applying interpolations during iterative phase retrieval, we conducted two numerical experiments, namely a "fatigue test" that repeatedly applying coordinate transformation and its inverse on a reconstructed object, and a "shuffle test" that alternating the sequence of Bragg peaks in the multiple-peak approach.

Fatigue test. This test is intended to reveal the numerical error that could accumulate during the iterative phasing process, due to the numerous interpolations. We use two error metrics to evaluate the error in the object. One is the σ-squared error metric, defined as

$$\sigma^2 = \frac{|\mathcal{F}(\rho_n) - \mathcal{F}(\rho_{initial})|^2}{|\mathcal{F}(\rho_{initial})|^2}, \#(A1)$$

where $\rho_{initial}$ is the initial object in the detector frame, ρ_n is the object in the detector frame after applying full coordinate transformation n times, and $\mathcal{F}$ denotes the Fourier transform operation. A full coordinate transformation includes two interpolations, one is from the detector frame to the crystal frame and the other is the inverse. Similar to the χ-squared error metric used to monitor the convergence of the phase retrieval algorithms, the σ-squared error metric tracks the change in Fourier magnitudes of the object after multiple interpolations. The other error metric tracks the marginal change in Fourier magnitudes. It is defined as

$$\eta^2 = \frac{|\mathcal{F}(\rho_n) - \mathcal{F}(\rho_{n-1})|^2}{|\mathcal{F}(\rho_{n-1})|^2}. \#(A2)$$

Fig. A2 demonstrates the behaviors of σ-squared and η-squared error metrics during the repeated coordinate transformations. In Fig. A2(a), the initial σ^2 values of all four peaks are around 0.001. The error metric increases rapidly in a few tens of coordinate transformations, then slows down after the σ^2 values are above 0.05. Fig. A2(b) shows the behavior of the η-squared error metric. The η^2 values start from the highest value around 0.001 and decrease to 10^{-6} rapidly in less than 100 transformations.

The behaviors of σ^2 demonstrated in Fig. A2(a) is consistent with the ones shown in Fig. 3. In Fig. 3(a), the χ^2 values decrease rapidly after ceasing the coordinate transformation in the individual phase retrieval at the 211th iteration, indicating that the numerical error from coordinate transformations increase the χ^2 values by approximately 0.002. This increment is close to the σ^2 values after one full coordinate transformation. Fig. 3(b) also shows a similar decrement at the 211th iteration, suggesting these interpolation-induced errors are independent of the strain-level of crystals.

Shuffle test. This test is aimed to investigate whether alternating the sequence of peaks in the multiple-peak approach affects the quality of obtained reconstructions. In this test, diffraction patterns of [002], [220], [311], and [111] were inverted in various sequences, using the multiple-peak approach with only ER for 220 iterations. For each sequence, the phase retrieval process was repeated 10 times with random seeds. No significant change in the reconstruction quality was

observed in the visual inspection. However, we find that the final χ^2 value of each peak depends on the previous peak. For example, in sequences [220] => [311] => [002] => [111] and [002] => [220] => [311] => [111], peak [311] has the identical final χ^2, while the other three peaks give different final χ^2 values. Table A1 summarizes the final χ^2 of each peak when it is reconstructed after different peaks. This interesting behavior suggests that the numerical error introduced by the multiple-peak approach is caused by a "mismatch" between two Bragg peaks, rather than the interpolation itself.

Appendix D: Computation requirement of the new workflow

A practical challenge of the new workflow is the computation time. It takes approximately 30 minutes for the new workflow to invert four 64 × 64 × 64 data arrays with 250 iterations of ER and HIO, because of the numerous interpolations. As a comparison, inverting one array using the conventional method takes only 57 seconds. However, phase retrieval from data in the case of highly-strained crystals is a difficult problem and usually requires a guided approach [47]. Typically, this involves tens of random starts and several generations. The resultant computational requirement commonly exceeds those of the new workflow.

The new workflow will also encounter the time consumption problem when the data arrays become larger. Since the interpolation has an $O(n)$ complexity, interpolating a 128 × 128 × 128 array takes about 4 seconds, in comparison with 0.5 second for a 64 × 64 × 64 array. As a result, the time consumption of the phase retrieval process will increase from minutes to hours. A workaround is binning the data array, which decreases the oversampling ratio. One can use the new workflow to invert the binned data arrays and acquire a reasonable support and crystal deformation. Then, the original array can be inverted in a conventional workflow, using the obtained support and the crystal deformation as the seed.

It is worth mentioning that the new workflow can invert diffraction datasets with different sampling conditions. One can adjust the spatial sampling rate and the largest scattering angle of a specific diffraction measurement, based on the complexities of the effective electron density and strain distributions. Although it requires an additional binning step during the multiple-peak phase retrieval process, this feature can accelerate the interpolations dramatically. Therefore, assigning non-uniform data collection conditions can significantly reduce the computation requirement.

References

[1] R. S. Jacobsen, K. N. Andersen, P. I. Borel, J. Fage-Pedersen, L. H. Frandsen, O. Hansen, M. Kristensen, A. V. Lavrinenko, G. Moulin, H. Ou, C. Peucheret, B. Zsigri, and A. Bjarklev, *Strained Silicon as a New Electro-Optic Material*, Nature **441**, 7090 (2006).
[2] P. Strasser, S. Koh, T. Anniyev, J. Greeley, K. More, C. Yu, Z. Liu, S. Kaya, D. Nordlund, H. Ogasawara, M. F. Toney, and A. Nilsson, *Lattice-Strain Control of the Activity in Dealloyed Core–Shell Fuel Cell Catalysts*, Nature Chemistry **2**, 6 (2010).
[3] R. Roldán, A. Castellanos-Gomez, E. Cappelluti, and F. Guinea, *Strain Engineering in Semiconducting Two-Dimensional Crystals*, J. Phys.: Condens. Matter **27**, 313201 (2015).
[4] I. K. Robinson, I. A. Vartanyants, G. J. Williams, M. A. Pfeifer, and J. A. Pitney, *Reconstruction of the Shapes of Gold Nanocrystals Using Coherent X-Ray Diffraction*, Phys. Rev. Lett. **87**, 195505 (2001).
[5] G. J. Williams, M. A. Pfeifer, I. A. Vartanyants, and I. K. Robinson, *Three-Dimensional Imaging of*

Microstructure in Au Nanocrystals, Phys. Rev. Lett. **90**, 175501 (2003).

[6] M. A. Pfeifer, G. J. Williams, I. A. Vartanyants, R. Harder, and I. K. Robinson, *Three-Dimensional Mapping of a Deformation Field inside a Nanocrystal*, Nature **442**, 63 (2006).

[7] I. Robinson and R. Harder, *Coherent X-Ray Diffraction Imaging of Strain at the Nanoscale*, Nature Materials **8**, 291 (2009).

[8] T. A. Pitts and J. F. Greenleaf, *Fresnel Transform Phase Retrieval from Magnitude*, IEEE Transactions on Ultrasonics, Ferroelectrics, and Frequency Control **50**, 1035 (2003).

[9] G. J. Williams, H. M. Quiney, B. B. Dhal, C. Q. Tran, K. A. Nugent, A. G. Peele, D. Paterson, and M. D. de Jonge, *Fresnel Coherent Diffractive Imaging*, Phys. Rev. Lett. **97**, 025506 (2006).

[10] T. Sun, Z. Jiang, J. Strzalka, L. Ocola, and J. Wang, *Three-Dimensional Coherent X-Ray Surface Scattering Imaging near Total External Reflection*, Nature Photonics **6**, 586 (2012).

[11] P. Thibault, M. Dierolf, A. Menzel, O. Bunk, C. David, and F. Pfeiffer, *High-Resolution Scanning X-Ray Diffraction Microscopy*, Science **321**, 379 (2008).

[12] S. O. Hruszkewycz, M. Allain, M. V. Holt, C. E. Murray, J. R. Holt, P. H. Fuoss, and V. Chamard, *High-Resolution Three-Dimensional Structural Microscopy by Single-Angle Bragg Ptychography*, Nature Materials **16**, 244 (2017).

[13] J. W. Miao, P. Charalambous, J. Kirz, and D. Sayre, *Extending the Methodology of X-Ray Crystallography to Allow Imaging of Micrometre-Sized Non-Crystalline Specimens*, Nature **400**, 342 (1999).

[14] H. N. Chapman, A. Barty, S. Marchesini, A. Noy, S. P. Hau-Riege, C. Cui, M. R. Howells, R. Rosen, H. He, J. C. H. Spence, U. Weierstall, T. Beetz, C. Jacobsen, and D. Shapiro, *High-Resolution Ab Initio Three-Dimensional x-Ray Diffraction Microscopy*, J. Opt. Soc. Am. A **23**, 1179 (2006).

[15] J. W. Miao, T. Ishikawa, I. K. Robinson, and M. M. Murnane, *Beyond Crystallography: Diffractive Imaging Using Coherent x-Ray Light Sources*, Science **348**, 530 (2015).

[16] J. R. Fienup, *Phase Retrieval Algorithms - a Comparison*, Applied Optics **21**, 2758 (1982).

[17] V. Elser, *Phase Retrieval by Iterated Projections*, J. Opt. Soc. Am. A **20**, 40 (2003).

[18] S. Marchesini, *Invited Article: A Unified Evaluation of Iterative Projection Algorithms for Phase Retrieval*, Review of Scientific Instruments **78**, 011301 (2007).

[19] M. C. Newton, R. Harder, X. Huang, G. Xiong, and I. K. Robinson, *Phase Retrieval of Diffraction from Highly Strained Crystals*, Phys. Rev. B **82**, 165436 (2010).

[20] X. Huang, R. Harder, G. Xiong, X. Shi, and I. Robinson, *Propagation Uniqueness in Three-Dimensional Coherent Diffractive Imaging*, Phys. Rev. B **83**, 224109 (2011).

[21] F. Hofmann, E. Tarleton, R. J. Harder, N. W. Phillips, P.-W. Ma, J. N. Clark, I. K. Robinson, B. Abbey, W. Liu, and C. E. Beck, *3D Lattice Distortions and Defect Structures in Ion-Implanted Nano-Crystals*, Scientific Reports **7**, 1 (2017).

[22] M. C. Newton, *Concurrent Phase Retrieval for Imaging Strain in Nanocrystals*, Phys. Rev. B **102**, 014104 (2020).

[23] Z. Wang, O. Gorobtsov, and A. Singer, *An Algorithm for Bragg Coherent X-Ray Diffractive Imaging of Highly Strained Nanocrystals*, New J. Phys. **22**, 013021 (2020).

[24] K. Lonsdale, *Extinction in X-Ray Crystallography*, Mineralogical Magazine and Journal of the Mineralogical Society **28**, 14 (1947).

[25] B. E. Warren, *X-Ray Diffraction* (Dover Publications, 2012).

[26] T. Schoonjans, A. Brunetti, B. Golosio, M. Sanchez del Rio, V. A. Solé, C. Ferrero, and L. Vincze, *The Xraylib Library for X-Ray–Matter Interactions. Recent Developments*, Spectrochimica Acta Part B: Atomic Spectroscopy **66**, 776 (2011).

[27] M. A. Pfeifer, Structural Studies of Lead Nanocrystals Using Coherent X-Ray Diffraction, PhD Thesis, University of Illinois at Urbana-Champaign, 2005.

[28] G. R. Wood, *The Bisection Method in Higher Dimensions*, Mathematical Programming **55**, 319 (1992).

[29] R. Penrose, *A Generalized Inverse for Matrices*, Mathematical Proceedings of the Cambridge

Philosophical Society **51**, 406 (1955).

[30] M. C. Newton, S. J. Leake, R. Harder, and I. K. Robinson, *Three-Dimensional Imaging of Strain in a Single ZnO Nanorod*, Nature Materials **9**, 120 (2010).

[31] S. Marchesini, H. He, H. N. Chapman, S. P. Hau-Riege, A. Noy, M. R. Howells, U. Weierstall, and J. C. H. Spence, *X-Ray Image Reconstruction from a Diffraction Pattern Alone*, Physical Review B **68**, 4 (2003).

[32] M. J. Cherukara, R. Pokharel, T. S. O'Leary, J. K. Baldwin, E. Maxey, W. Cha, J. Maser, R. J. Harder, S. J. Fensin, and R. L. Sandberg, *Three-Dimensional X-Ray Diffraction Imaging of Dislocations in Polycrystalline Metals under Tensile Loading*, Nature Communications **9**, 3776 (2018).

[33] F. Hofmann, N. W. Phillips, S. Das, P. Karamched, G. M. Hughes, J. O. Douglas, W. Cha, and W. Liu, *Nanoscale Imaging of the Full Strain Tensor of Specific Dislocations Extracted from a Bulk Sample*, Phys. Rev. Materials **4**, 013801 (2020).

[34] A. Ulvestad, A. Singer, H. M. Cho, J. N. Clark, R. Harder, J. Maser, Y. S. Meng, and O. G. Shpyrko, *Single Particle Nanomechanics in Operando Batteries via Lensless Strain Mapping*, Nano Letters **14**, 5123 (2014).

[35] P. Ovartchaiyapong, K. W. Lee, B. A. Myers, and A. C. B. Jayich, *Dynamic Strain-Mediated Coupling of a Single Diamond Spin to a Mechanical Resonator*, Nature Communications **5**, 4429 (2014).

[36] S. O. Hruszkewycz, S. Maddali, C. P. Anderson, W. Cha, K. C. Miao, M. J. Highland, A. Ulvestad, D. D. Awschalom, and F. J. Heremans, *Strain Annealing of SiC Nanoparticles Revealed through Bragg Coherent Diffraction Imaging for Quantum Technologies*, Phys. Rev. Materials **2**, 086001 (2018).

[37] J. R. Petrie, V. R. Cooper, J. W. Freeland, T. L. Meyer, Z. Zhang, D. A. Lutterman, and H. N. Lee, *Enhanced Bifunctional Oxygen Catalysis in Strained LaNiO3 Perovskites*, J. Am. Chem. Soc. **138**, 2488 (2016).

[38] D. Sayre, *Some Implications of a Theorem Due to Shannon*, Acta Cryst **5**, 843 (1952).

[39] J. Miao, D. Sayre, and H. N. Chapman, *Phase Retrieval from the Magnitude of the Fourier Transforms of Nonperiodic Objects*, J. Opt. Soc. Am. A **15**, 1662 (1998).

[40] H Öztürk and X Huang and H Yan and I K Robinson and I C Noyan and Y S Chu, *Performance Evaluation of Bragg Coherent Diffraction Imaging*, New Journal of Physics **19**, 103001 (2017).

[41] Q. Shen, I. Bazarov, and P. Thibault, *Diffractive Imaging of Nonperiodic Materials with Future Coherent X-Ray Sources*, J Synchrotron Rad **11**, 432 (2004).

[42] J.-P. Liu, *Controlling the Aliasing by Zero-Padding in the Digital Calculation of the Scalar Diffraction*, J. Opt. Soc. Am. A, JOSAA **29**, 1956 (2012).

[43] A. I. Pateras, Three Dimensional X-Ray Bragg Ptychography of an Extended Semiconductor Heterostructure, PhD Thesis, Aix Marseille University, 2015.

[44] D. Yang, N. W. Phillips, and F. Hofmann, *Mapping Data between Sample and Detector Conjugated Spaces in Bragg Coherent Diffraction Imaging*, J Synchrotron Rad **26**, 6 (2019).

[45] S. Maddali, P. Li, A. Pateras, D. Timbie, N. Delegan, A. L. Crook, H. Lee, I. Calvo-Almazan, D. Sheyfer, W. Cha, F. J. Heremans, D. D. Awschalom, V. Chamard, M. Allain, and S. O. Hruszkewycz, *General Approaches for Shear-Correcting Coordinate Transformations in Bragg Coherent Diffraction Imaging. Part I*, J Appl Cryst **53**, 2 (2020).

[46] P. Li, S. Maddali, A. Pateras, I. Calvo-Almazan, S. O. Hruszkewycz, W. Cha, V. Chamard, and M. Allain, *General Approaches for Shear-Correcting Coordinate Transformations in Bragg Coherent Diffraction Imaging. Part II*, J Appl Cryst **53**, 2 (2020).

[47] C.-C. Chen, J. Miao, C. W. Wang, and T. K. Lee, *Application of Optimization Technique to Noncrystalline X-Ray Diffraction Microscopy: Guided Hybrid Input-Output Method*, Phys. Rev. B **76**, 064113 (2007).

Tables

TABLE I. Success rate of phase retrieval in high-strain cases (screw dislocation along x' direction).

	Bragg peak(s)	Trials	Success Rate
IP	[022]	20	100%
	[002]	20	100%
	[$\overline{1}\overline{1}\overline{1}$]	20	90%
	[200]	20	0%
	[311]	20	0%
MP	[022] [$\overline{1}\overline{1}\overline{1}$] [002] [020]	10	100%
	[022] [200] [002] [020]	10	50%
	[022] [$\overline{1}\overline{1}\overline{1}$] [002] [200]	10	70%
	[022] [$\overline{1}\overline{1}\overline{1}$] [002] [311]	10	60%
	[022] [200] [002] [311]	10	30%

TABLE A1. Final χ^2 values of [002], [220], [311], and [111] reconstructed in different sequences.

	After [002]	After [220]	After [311]	After [111]
[002]	-	0.0821 ± 0.0009	0.0184 ± 0.0005	0.0052 ± 0.0004
[220]	0.0544 ± 0.0006	-	0.0210 ± 0.0005	0.0456 ± 0.0006
[311]	0.0173 ± 0.0003	0.0233 ± 0.0003	-	0.0124 ± 0.0002
[111]	0.0079 ± 0.0004	0.0686 ± 0.0009	0.0157 ± 0.0006	-

Figures
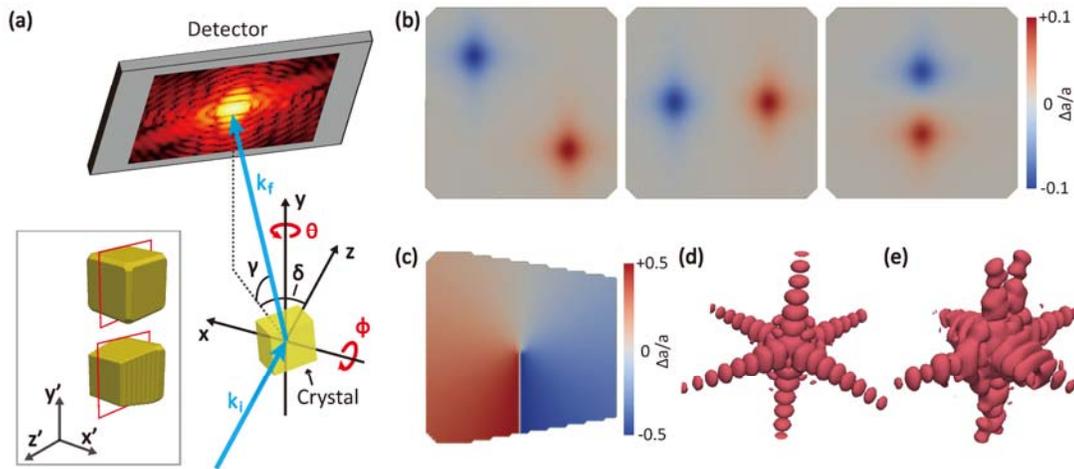
FIG. 1. Schematic diagram of the simulated diffraction. (a) A typical diffraction geometry in a right-handed coordinate system with z in the direction of the propagation of the incident X-ray beam. k_i and k_f are the wavevectors of incident and diffracted X-ray photons, respectively. θ and φ are the diffractometer angles, while δ and γ are the detector angles. (Inset) Simulated crystals in the crystal frame (i.e. x', y', and z'). (b) Lattice deformation within a cubic crystal along x' (left), y' (middle), and z' (right) directions, on the plane defined by the red square shown in (a) inset. (c) Screw dislocation within a frustum-shaped crystal along x' direction. (d) and (e) show the [111] Bragg peak from the two crystals, respectively.
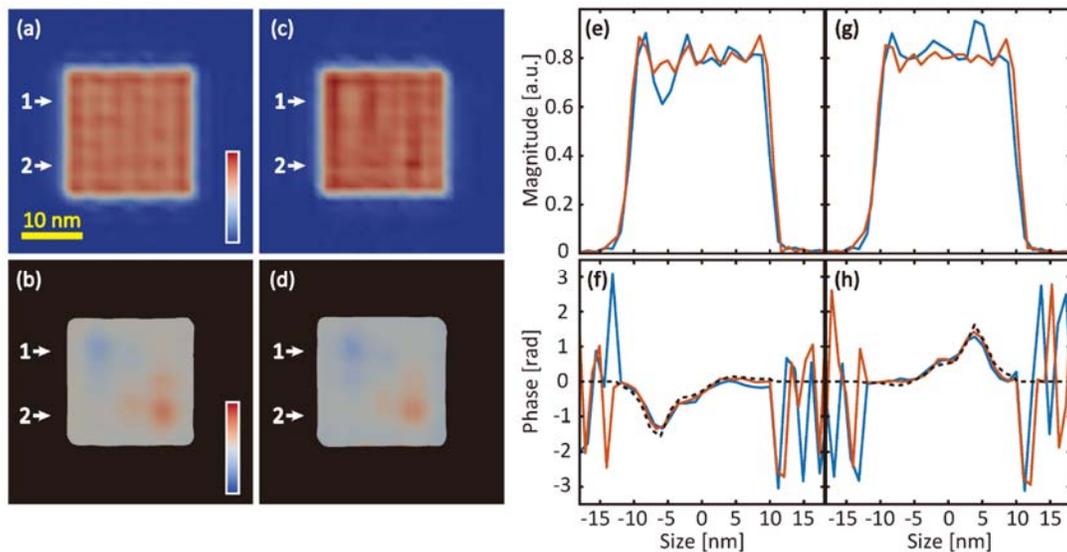
FIG. 2. Reconstruction of [311] peak using different approaches. (a) and (b) are the magnitude and phase of the object obtained from the multiple-peak approach, while the ones retrieved from individual peak approach are shown in (c) and (d). The phase maps are masked by the isosurface level of 30%. The color bars are from 0 to 1 in (a), and from -π to π in (b). (e) and (g) are the magnitude lineouts along horizontal lines at the locations marked by 1 and 2, respectively. Red lines are from (a) and blue lines are from (c). Similarly, (f) and (h) are the phase lineouts from (b) and (d). The dashed lines in (f) and (h) show the phase changes estimated from the deformation in the truth object.
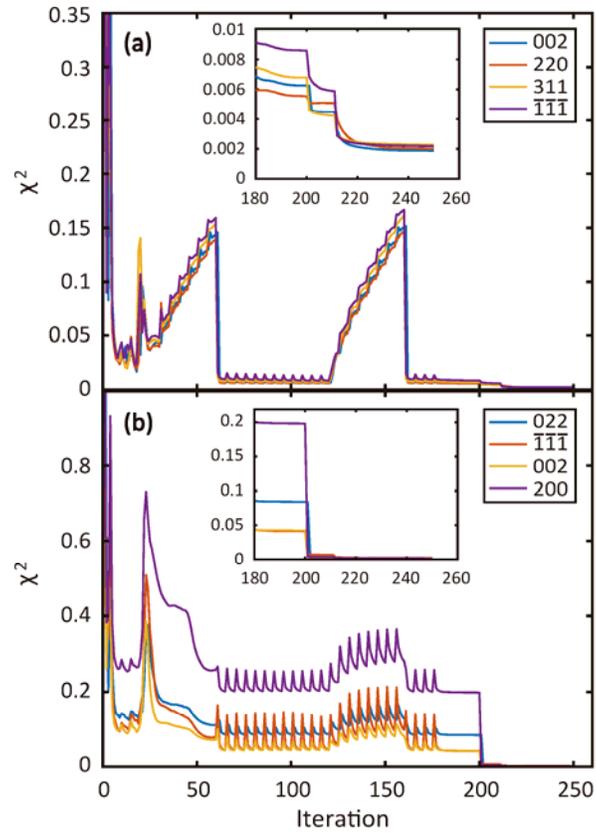
FIG. 3. The χ^2 error metric during multiple-peak phase retrieval for the low-strain case (a) and the high-strain case (b). For both cases, χ^2 values from the 180th iteration to the 250th iteration are shown in the insets.
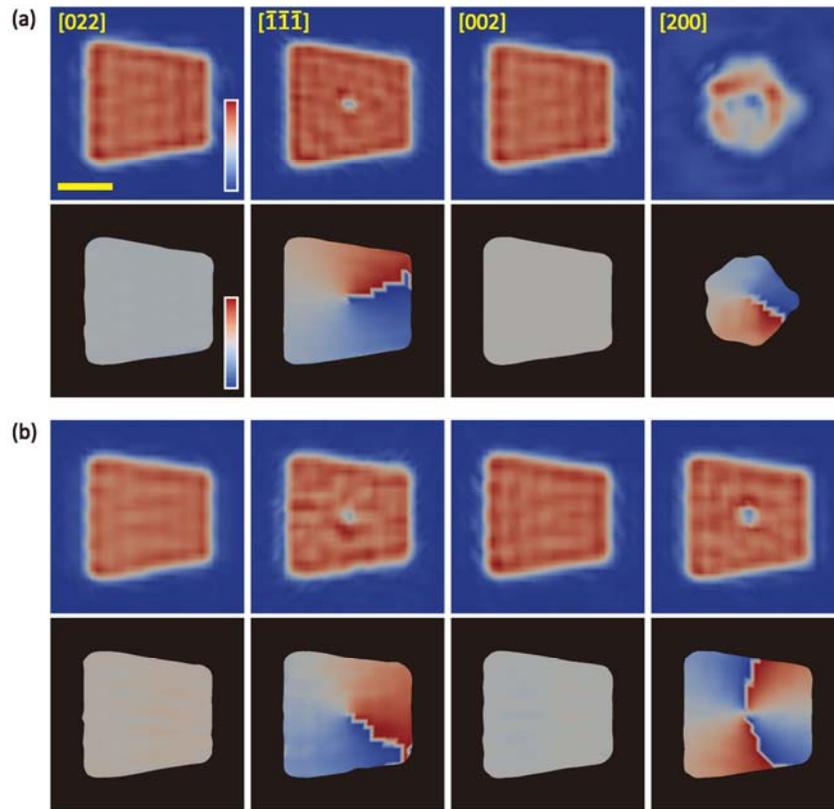
FIG. 4. Reconstructions from [022], [$\bar{1}\bar{1}\bar{1}$], [002], and [200] of a crystal with a screw dislocation, using individual-peak approach (a) and multiple-peak approach (b). The phase maps are masked by the isosurface level of 30%. The scale bar is 10 nm in length. The color bars are from 0 to 1 for magnitude, and from -π to π for phase.
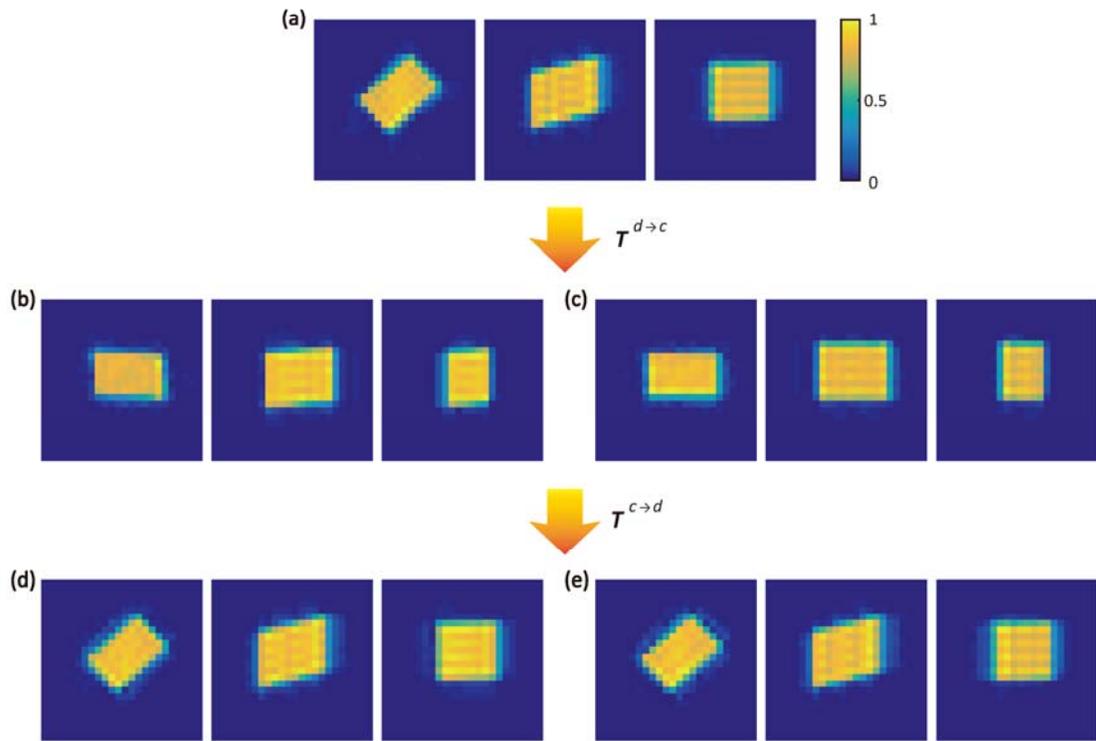
FIG. A1. Coordinate transformation of a reconstructed object between detector frame and crystal frame. (a) The object in the detector frame, obtained by directly inverting the [111] diffraction from a rectangular-prism-shaped crystal. Three slices through the center of the object along x-z (left), y-z (middle), and x-y (right) planes are shown. (b) and (d) show the object after applying coordinate transformation and the inverse transformation, while the Ewald sphere is approximated to a flat plane. (c) and (e) are similar to (b) and (d), respectively. However, the curvature of the Ewald sphere is taken into account while calculating the coordinates of grid points.
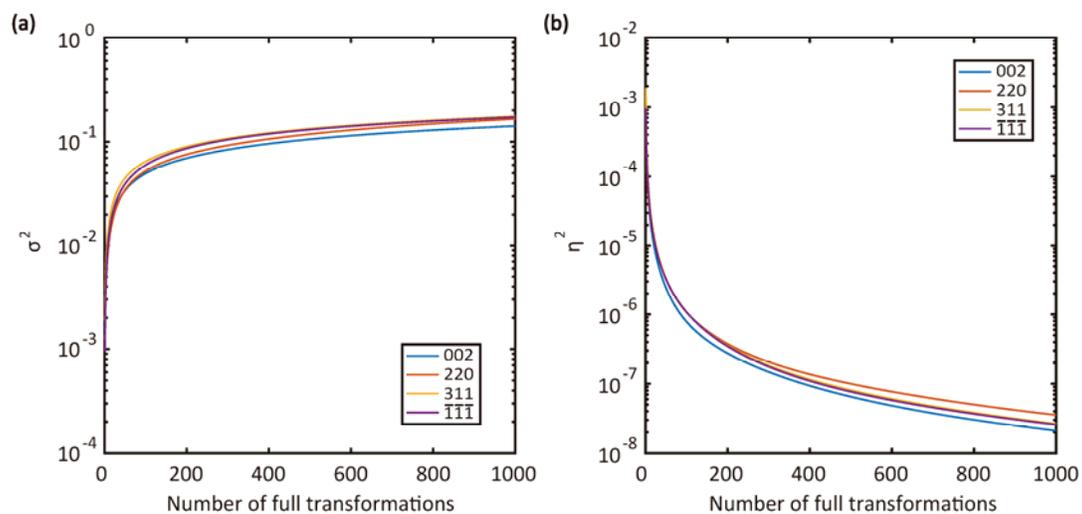
FIG. A2. Behaviors of (a) σ-squared and (b) η-squared error metrics during the repeated coordinate transformations. Each full transformation contains two interpolations, one from detector frame to crystal frame and the other is the inverse.
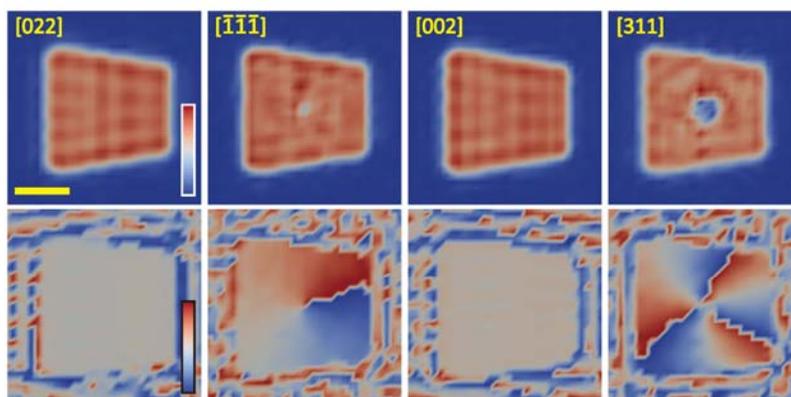
FIG. A3. Reconstructions from [022], [$\bar{1}\bar{1}\bar{1}$], [002], and [311] of a crystal with a screw dislocation, using the multiple-peak approach. The scale bar is 10 nm in length. The color bars are from 0 to 1 for magnitude, and from $-\pi$ to π for phase.
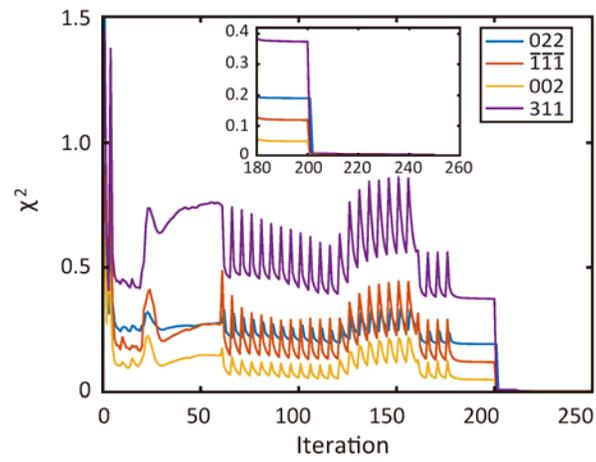
FIG. A4. χ-squared error metric during multiple-peak phase retrieval for high-strain case, using [022], [$\overline{1}\overline{1}\overline{1}$], [002], and [311]. Inset: χ^2 values from the 180th iteration to the 250th iteration.